A dynamic observer to capture and control perturbation energy in noise amplifiers

Juan Guzmán Iñigo[1], Denis Sipp[1] and Peter J. Schmid[2]

[1]ONERA-DAFE, 8 rue des Vertugadins, 92190 Meudon, France

[2]Dept. of Mathematics, Imperial College London, London SW7 2AZ, United Kingdom

(Received ?; revised ?; accepted ?.)

In this article we introduce techniques to build a reduced-order model of a fluid system which accurately predicts the dynamics of a flow from local wall measurements. This is particularly difficult in the case of noise amplifiers where the upstream noise environment, triggering the flow via a receptivity process, is not known. A system-identification approach, rather than a classical Galerkin technique, is used to extract the model from time-synchronous velocity snapshots and wall-shear stress measurements. The technique will be illustrated on the case of a transitional flat-plate boundary layer, where the snapshots of the flow are obtained from direct numerical simulations. Particular attention is directed to limiting the processed data to data that would be readily available in experiments, thus making the technique applicable to an experimental setup. The proposed approach combines a reduction of the degrees of freedom of the system by a projection of the velocity snapshots onto a POD basis combined with a system-identification technique to obtain a state-space model. This model is then used in a feedforward control setup to significantly reduce the kinetic energy of the perturbation field and thus successfully delay transition.

1. Introduction

Fluid systems that fall under the category of noise amplifiers are characterized by a globally stable spectrum despite the presence of convective instabilities. Boundary layers are examples of this type of fluid behavior. External perturbations permeate the near-wall region during the receptivity phase and initiate disturbances that are amplified into Tollmien-Schlichting waves as they are swept downstream. If these instabilities reach sufficient amplitudes, breakdown of the flow into turbulent fluid motion can occur. Much effort has been expended to understand and control this breakdown into turbulence by manipulating the underlying instability processes.

While many open-loop control techniques have been developed to delay the transition process, closed-loop approaches, where actuation depends on sensor measurements, are more effective and efficient (Kim & Bewley 2007). However, under realistic flow conditions, the direct application of closed-loop control techniques is often not tractable. The high degrees of freedom of fluid systems (often $\mathcal{O}(10^6)$) are far beyond the capabilities of current control devices which typically can handle $\mathcal{O}(10^2)$ variables. As a consequence, the full fluid system has to be properly reduced, before a controller can be designed for the reduced-order model. This methodology has been demonstrated to yield successful control designs, see Bagheri *et al.* (2009) and Barbagallo *et al.* (2009), among others. In these investigations, model reduction is accomplished by a flow decomposition (e.g., POD or BPOD decomposition) followed by a Galerkin projection of the equations onto the reduced basis.

In the case of noise amplifiers, external perturbations strongly influence the system dynamics. Thus, it is very important for the reduced-order model (ROM) to accurately capture the noise environment. In particular, ROMs obtained by means of Galerkin projections require detailed knowledge of the spatial distribution of the upstream noise sources. This requirement imposes great limitations, especially in experimental situations where information about the noise environment is neither directly nor sufficiently available. A promising alternative to control design based on Galerkin projections derives from system-identification techniques as proposed in Hervé *et al.* (2012); this approach also constitutes an encouraging step towards the control of noise amplifiers in experimental situations.

This paper intends to provide a methodology to obtain reduced-order estimators for noise amplifiers without using Galerkin projections. While in Hervé *et al.* (2012) the model describes only the dynamics between one sensor (upstream measurement) to another (downstream measurement), here we aim to capture the dynamics between upstream measurements and the *entire* perturbation field. This will allow the reconstruction of the full flow field and, consequently, the design of controllers that target the kinetic energy of the full perturbation field, not only the variance of a wall-measurement signal. This reminds the Galerkin-based output projection technique introduced by Rowley (2005) that captures the full perturbation field from a given input. However, the latter technique requires precise knowledge of the spatial distribution of the input, which is generally not available in amplifier flows. Therefore, Dergham *et al.* (2013) has extended it to also account for any possible input, so as to obtain a model that captures any input to any output. In the present work, we aim at obtaining a similar model — capturing the dynamics from unknown input to any output — but with identification methods. The proposed approach consists of a reduction of the degrees of freedom of the system by (i) a projection of the velocity fields onto a reduced basis combined with (ii) a system-identification algorithm to obtain the dynamic operators of a reduced-order system. In particular, a link between velocity fields (e.g., from TR-PIV data) and time-synchronous wall-shear stress measurements is established, and a dynamic observer is determined. A key feature of our procedure is its reliance on a Galerkin model *structure* but on the determination of the model matrices by system identification rather than integral expressions (Galerkin projections).

The link between velocity fields and wall measurements is reminiscent of linear stochastic estimation (LSE) techniques (Adrian 1979; Guezennec 1989; Bonnet *et al.* 1994; Tinney *et al.* 2006; Hudy *et al.* 2007; Taylor & Glauser 2004; Tu *et al.* 2013) where multiple, measured inputs are correlated to simultaneous, multiple outputs by averaging over many realizations. Our proposed technique generalizes this *static* approach by accounting for the *dynamics* of either measurement data. The comparison between LSE and dynamic observers obtained by Galerkin projection has already been considered in Rowley & Juttijudata (2005) showing the superiority of dynamic estimators. A further relation can be demonstrated to data-assimilation techniques, specifically, to the online variant (see, e.g., Lewis *et al.* 1989) where streaming data are matched to an underlying model which is then used to predict future measurement signals. Once a model has been extracted by our technique from measured data, it can straightforwardly be used in a closed-loop control application, as will be illustrated below.

The present study is structured as follows. After a brief description of the flow configuration and the governing equations (§ 2) we present a dynamic observer obtained by Galerkin projection (§ 3) and by the identification procedure (§ 4). § 5 will compare the identified observer with different well-known approaches, while § 6 will demonstrate how to include the identified model in a control framework. A summary of results and

conclusions are given in § 7. The appendix gives details about the employed subspace system identification techniques.

2. Problem formulation

2.1. *Governing equations*

We choose a zero-pressure gradient boundary layer — a classical and generic flow that acts as a noise amplifier — as our configuration to design and test the dynamic observer. This flow is globally stable but selectively amplifies upstream disturbances by convective instabilities. In a low-amplitude noise environment, two-dimensional Tollmien-Schlichting waves appear as a result of this instability mechanism.

We consider the dynamics of disturbances $\mathbf{u}$ around a base-flow $\mathbf{U}_0$, which we take as a Blasius boundary layer. The disturbances $\mathbf{u}$ are additionally driven by an external forcing term, $\mathbf{F}_w w(t)$, which acts as an upstream disturbance source of unknown origin. For simplicity, we assume that $w(t)$ is a random process of zero mean and variance W, while $\mathbf{F}_w$ describes a spatial two-dimensional Gaussian distribution centered at (x_w, y_w) of spread (σ_x, σ_y) and amplitude A. The spatio-temporal evolution of the total flow field, $\mathbf{U}_{\text{tot}} = \mathbf{U}_0 + \mathbf{u}$, is governed by the incompressible Navier-Stokes equations, augmented by a forcing term,

$$\partial_t \mathbf{U}_{\text{tot}} + \mathbf{U}_{\text{tot}} \cdot \nabla \mathbf{U}_{\text{tot}} = -\nabla P_{\text{tot}} + Re_{\delta_0^*}^{-1} \Delta \mathbf{U}_{\text{tot}} + \mathbf{F}_w w(t), \qquad \nabla \cdot \mathbf{U}_{\text{tot}} = 0. \quad (2.1)$$

The variables are non-dimensionalized using the displacement thickness δ_0^* of the boundary-layer at the computational inlet ($x_0 = 0$) and the free-stream velocity U_∞. Consequently, the Reynolds number is defined as $Re_{\delta_0^*} = U_\infty \delta_0^* / \nu$. All simulations were performed at $Re_{\delta_0^*} = 1000$, which ensures the presence of strong Tollmien-Schlichting instabilities since $Re_{\delta_0^*} > Re_{\delta^*}^{\text{crit}} = 520$.

The governing equations (2.1) are solved in a computational domain Ω of size $(0, 1000) \times (0, 40)$, sketched in figure 1. A Blasius profile of unit displacement thickness is prescribed at the left boundary, outflow conditions are employed at the upper and right boundaries, and a no-slip condition is imposed at the wall. We use the spectral-element code `Nek5000` (see https://nek5000.mcs.anl.gov) to perform the computations below.

With the base flow $\mathbf{U}_0$ as a solution of the unforced ($w = 0$) steady Navier-Stokes equations (2.1), the perturbations $\mathbf{u}$ are governed by the following equations

$$\partial_t \mathbf{u} + \mathbf{U}_0 \cdot \nabla \mathbf{u} + \mathbf{u} \cdot \nabla \mathbf{U}_0 = -\nabla p + Re_{\delta_0^*}^{-1} \Delta \mathbf{u} + \mathbf{F}_w w(t), \qquad \nabla \cdot \mathbf{u} = 0, \quad (2.2)$$

where the nonlinear term $\mathbf{u} \cdot \nabla \mathbf{u}$ has been omitted since only low-amplitude noise $W \ll 1$ will be considered. This assumption ensures linear perturbation dynamics, as well as a linear response to the noise w. During the DNS simulations, white noise is imposed via $w(n)$ to mimic upstream excitations of unknown source and distribution (mimicking conditions in physical experiments). We use a time-step of $dt_{\text{dns}} = 0.1$.

2.2. *Perturbation dynamics*

Choosing the Blasius boundary layer as an example of a noise amplifier and assuming a low-noise environment, perturbations may be amplified by two different instability mechanisms: (i) the Tollmien-Schlichting instability which takes advantage of a critical layer as well as a wall layer to generate a non-zero Reynolds stress, and (ii) the Orr instability where initial perturbations lean against the mean shear but grow in amplitude as they are tilted by the mean velocity (Butler & Farrell 1992). The details of these mechanisms can be studied within a local stability framework, considering perturbations

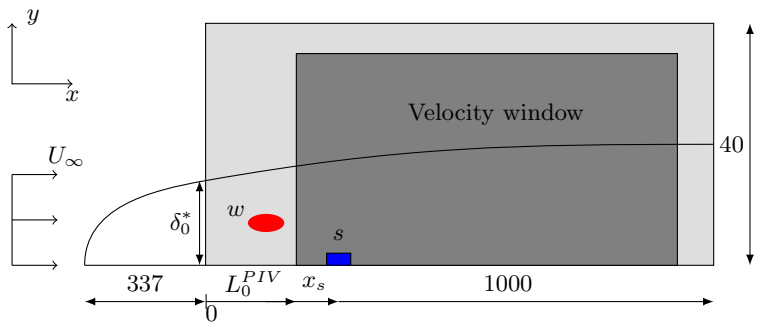

Figure 1: Sketch of the flow configuration. The computational domain Ω is of size $(0, 1000) \times (0, 40)$, represented by the light gray box. The upstream receptivity of the boundary layer to external perturbations is modeled by the noise w which is placed at $(x_w, y_w) = (50, 0.95)$. A sensor located at $(x_s, y_s) = (200, 0)$ will identify incoming perturbations, while a velocity window (represented by the dark gray box) is used to quantify the effect of the forcing on the velocity field.

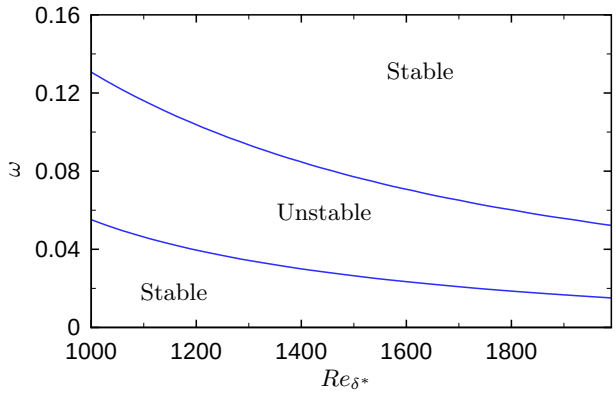

Figure 2: Neutral curve obtained by a local spatial stability analysis in the computational domain.

of the form $e^{i(\alpha x - \omega t)}$, with ω as the frequency and α as the streamwise wavenumber of the perturbation. An analysis of this type shows that the Blasius boundary layer is convectively unstable to Tollmien-Schlichting waves when the Reynolds number based on the local displacement thickness $\delta^*(x)$ is larger than the critical value of $Re = 520$. In figure 2, the neutral curve obtained from a local spatial stability analysis performed with wall-normal profiles extracted from the base flow $\mathbf{U}_0$ is displayed. The unstable frequencies fall in the interval $0.055 < \omega < 0.13$ at the computational inlet and $0.015 < \omega < 0.052$ at the end of the domain. When a localized disturbance is placed inside the boundary layer, the response is a wavepacket which convects downstream at the local group velocity $v_g = d\omega/d\alpha$. The group velocity is a very important parameter, as it sets a characteristic time for the perturbation, and can easily be obtained from the dispersion relation $\omega = \omega(\alpha)$. In figure 3, the dispersion relation is represented for three different Reynolds numbers (corresponding to streamwise locations at the computational inlet, middle and outlet). For the considered configuration, the group velocity is estimated as $v_g \approx 0.375 U_\infty$ using the real-axis approximation.

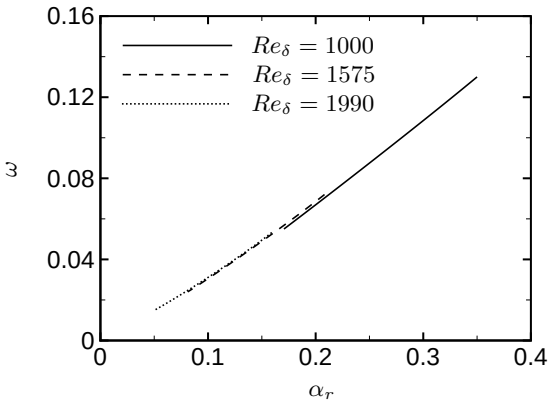

Figure 3: Spatial dispersion relation for the convectively unstable frequencies at three different positions within the domain.

2.3. *Measurements*

This paper aims at providing a data-based technique that is applicable in an experimental setting. For this reason, special care must be taken to only use data which is readily available in an experiment. We first consider a wall-friction sensor s (see figure 1), located at $x_s = 200$ and of spatial extension in the streamwise direction $\Delta x = 0.5$, which measures the wall shear-stress:

$$s_{\text{tot}} = \int_{x_s}^{x_s+\Delta x} \left.\frac{\partial u_{\text{tot}}}{\partial y}\right|_{y=0} dx + g = \int_{x_s}^{x_s+\Delta x} \left.\frac{\partial U_0}{\partial y}\right|_{y=0} dx + \underbrace{\int_{x_s}^{x_s+\Delta x} \left.\frac{\partial u}{\partial y}\right|_{y=0} dx + g}_{s(t)}, \tag{2.3}$$

where s denotes the fluctuating part of the measurement, which may be obtained by subtracting the time-averaged value of s_{tot} from the signal s_{tot}. For the case of low-amplitude forcing, i.e., for linear perturbation dynamics, the time-averaged value also corresponds to the base-flow value. The sensor s_{tot} (or s) may be corrupted by white noise g, of variance G (with G small and of the order of magnitude of W).

In addition to the wall-friction sensor s, we also consider velocity snapshots $\mathbf{u}_{\text{snap}}$ in a given domain Ω_{snap}, which may be chosen smaller than the computational domain Ω (see figure 1). The fluctuating parts of the velocity field may again be obtained by subtracting the time-averaged snapshots from the total snapshot sequence. In an experimental setup, the velocity snapshots may be obtained by a PIV technique. In what follows, we will consider time-series of composite skin-friction measurements and velocity snapshots.

3. Structure of a dynamic observer using Galerkin projection

In this section the model reduction technique based on Galerkin projection will be briefly discussed to motivate the use of identification methods in the design of reduced-order models (ROMs). Special attention will be paid to the structure of the resulting model since it will form the basis of the system-identification approach. We proceed by developing and analyzing the ROM that would result from a projection of the linearized Navier-Stokes equations onto a POD basis (§ 3.1) which is followed by the introduction

of a Kalman filter allowing us to replace the unknown driving term $w(t)$ by the known measurements $s(t)$ (§ 3.2).

3.1. *Reduced-order model with Galerkin projection by approximation of the controllability Gramian*

A common method used to obtain a reduced-order model of a dynamical system is based on Galerkin projection, i.e., a projection of the Navier-Stokes equations (2.2) onto an appropriate basis, such that the input-output behavior of the full system is preserved as accurately as possible. The choice of basis is critical. The two most common options are based on: an approximation of the controllability Gramian which yields a POD basis (Rowley 2005; Barbagallo *et al.* 2009) that maximizes the energy captured by the reduced-order model, and an approximation of the controllability and observability Gramians which yields a balanced basis (Moore 1981; Rowley 2005; Bagheri *et al.* 2009) that directly focuses on the input-output relation of the reduced system. In this article, only ROMs obtained by approximating the controllability Gramian will be considered.

After extracting the POD modes (taking data from the full computational domain) from the approximation of the controllability Gramian by an impulse response of the full system (see Barbagallo *et al.* (2009) for details), the governing equations (2.2) are projected onto the first k modes to obtain a reduced state-space representation of the system according to

$$\frac{d\mathbf{X}}{dt} = \mathsf{A}'_w \mathbf{X}(t) + \mathbf{B}'_w w(t), \tag{3.1a}$$

$$s(t) = \mathbf{C}'\mathbf{X}(t) + g(t). \tag{3.1b}$$

where $\mathbf{X}(t)$ is a vector containing the k POD coefficients at time t. Denoting by $\langle\cdot\rangle$ the energy based-inner product that has been used to extract the POD modes, the components of the matrix A'_w and of the vectors $\mathbf{B}'_w$, $\mathbf{C}'$ are obtained as follows: $\mathsf{A}'_{w,ij} = \langle \mathbf{\Phi}_i, \mathscr{A}\mathbf{\Phi}_j \rangle$ (with $\mathscr{A}$ as the linearized Navier-Stokes operator (2.2) on Ω), $\mathbf{B}'_{w,i} = \langle \mathbf{\Phi}_i, \mathbf{F}_w \rangle$ and $\mathbf{C}'_i = \mathscr{C}\mathbf{\Phi}_i$ (with $\mathscr{C}$ as the measurement operator).

A Galerkin projection usually provides a continuous-time format for the state-space system (3.1). With the remaining article pertaining to system identification methods, it is more convenient to express the governing equations in a discrete-time framework. In the discrete-time domain, the mapping of the state-vector $\mathbf{X}$ from time t (index n) to $t + \Delta t$ (index $n+1$) reads

$$\mathbf{X}(n+1) = \mathsf{A}_w \mathbf{X}(n) + \mathbf{B}_w w(n), \tag{3.2a}$$

$$s(n) = \mathbf{C}\mathbf{X}(n) + g(n), \tag{3.2b}$$

with $\mathbf{B}_w = \int_0^{\Delta t} \exp[\mathsf{A}'_w(\Delta t - \tau)]\mathbf{B}'_w \, d\tau$ associated with the discrete driving term, $\mathsf{A}_w = \exp(\mathsf{A}'_w \Delta t)$ denoting the evolution matrix over a time interval Δt and $\mathbf{C} = \mathbf{C}'$.

3.2. *Kalman filter*

When dealing with noise amplifiers, it is critical to accurately account for the disturbance environment, as it both triggers and sustains the dynamics of the system. Despite this requirement, in an experimental setup, access to accurate information about the noise environment is, at best, very difficult or, in most cases, impossible. We thus have to introduce an observer where the noise source-term $\mathbf{B}_w w(t)$ is replaced by a measurement term $\mathbf{L}s(t)$ which drives, as best as possible, the estimated state of the system. Formally, the observer may be obtained in a straightforward manner by introducing a linear estimator

of the form

$$\mathbf{X}_e(n+1) = \mathsf{A}_w \mathbf{X}_e(n) + \mathbf{L}\left[s(n) - \mathbf{C}\mathbf{X}_e(n)\right] = \mathsf{A}_s \mathbf{X}_e(n) + \mathbf{L}s(n), \tag{3.3}$$

where $\mathbf{X}_e(n)$ is the estimated state, $s(n)$ is the measurement signal from the friction sensor (defined by (2.3)) and $\mathbf{L}$ represents the gain of the estimator which can be selected by the designer to achieve different objectives. If the gain $\mathbf{L}$ is selected to statistically minimize the error $\|\mathbf{X}_e - \mathbf{X}\|_2$, the estimator is referred to as a Kalman filter and $\mathbf{L}$ is obtained by solving a Riccati equation (see Burl (1999)) of the form

$$\mathsf{P} = \mathsf{A}_w \mathsf{P} \mathsf{A}_w^* - \mathsf{A}_w \mathsf{P} \mathbf{C}^* \left(\mathbf{C}\mathsf{P}\mathbf{C}^* + G\right)^{-1} \mathbf{C}\mathsf{P}\mathsf{A}_w^* + \mathbf{B}_w W \mathbf{B}_w^*, \tag{3.4a}$$

$$\mathbf{L} = \mathsf{A}_w \mathsf{P} \mathbf{C}^* \left(\mathbf{C}\mathsf{P}\mathbf{C}^* + G\right)^{-1}. \tag{3.4b}$$

In short, the dynamic observer (3.3) consists of a linear relationship between two subsequent state-vectors $\mathbf{X}_e(n+1), \mathbf{X}_e(n)$ and the measurement $s(n)$. Its dynamics are fully determined by the evolution matrix $\mathsf{A}_s = \mathsf{A}_w - \mathbf{L}\mathbf{C}$ and the observer gain $\mathbf{L}$. We stress that this estimator is effective, only if the measurement s remains constant over the sampling time Δt; for this reason, a spectral analysis of the measurement s must be employed to determine its frequency content and thus the sampling time Δt.

3.3. *Limitations of Galerkin-based methods*

Galerkin models based on Gramians are a popular choice for model reduction, owing to their ease of use in feedback applications, the availability of mathematical bounds on their convergence, and their link to physically relevant flow structures. But despite their wide-spread use, Galerkin-based methods for the computation of reduced-order models suffer from notable limitations when they are applied to experimental situations.

The favorable properties of the Galerkin model presented in this section stem from the fact that the POD modes were obtained by accurately discretizing the integral involved in the controllability Gramian. This requires that an impulse of $w(t)$ can be generated and its response can be analyzed using velocity snapshots; furthermore, a very small delay between two successive snapshots and a very long series of snapshots is desirable. If such requirements are not met, Galerkin projection then provides POD-based models which may even become unstable: *a posteriori* regularization and calibration techniques are then required to render the models stable again (Bergmann *et al.* (2009)).

One of the most important limitations of Galerkin-based models is linked to the requirement of a very accurate distribution of the noise sources in the experiment for amplifier flows, since these sources will drive the dynamics of the system. Generally, the noise distribution in experimental setups will be complex, difficult to represent, and mostly unknown, so that triggering by an impulse in $w(t)$ is nearly impossible.

4. Dynamic observer using system-identification techniques

This section introduces an alternative method to obtain a dynamic observer. We will present a data-driven approach, based on system identification techniques, that solely relies on observations of the system in the presence of unknown upstream noise $w(t)$. System identification techniques represent a family of algorithms which efficiently determine the coefficients of an underlying model directly from observed input-output data via a statistical learning process. This section aims at obtaining a dynamic observer model such as Eq. (3.3) directly from observations of the system. In the following, we will first briefly recall the basics of system identification techniques, which generate a

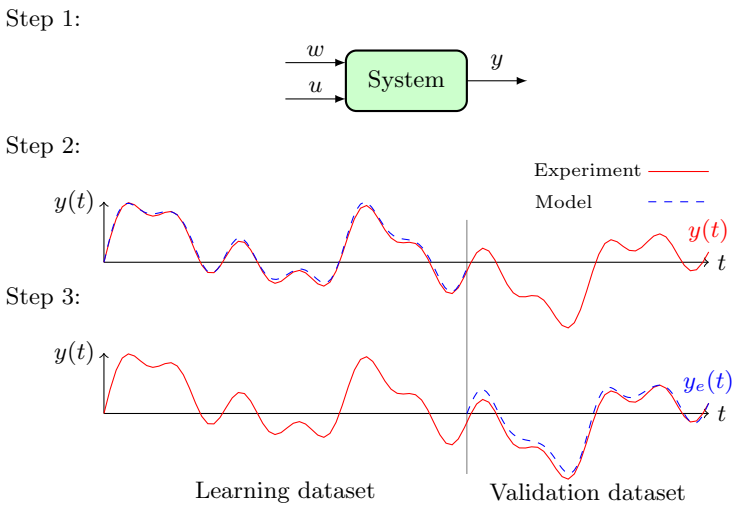

Figure 4: Procedural steps of system identification techniques. Step 1: The system is forced with a frequency-rich input signal and data is acquired. The forcing term $w(n)$ driving the system should be either known, or replaced by a known proxy measurement $s(n)$. Step 2: After selecting a model structure and appropriate parameters, the model coefficients are then computed by maximizing the fit between the output of the system and the prediction of the model for a part of the available data. Step 3: The model is tested on a dataset different than the one used for learning. If the model does not reproduce the system dynamics with the required accuracy, a different model structure, a different parametrization or even a different experiment should be considered.

model governing the dynamics of given outputs from known inputs (§4.1). Second, we will define the output of our system as the coefficients of the velocity snapshots in a POD basis (§4.2). Third, we will introduce the model structure of the dynamic observer (§4.3), identify the coefficients of the model (§4.4) and validate the model (§4.5). Finally, the influence of various parameters on the quality of the model will be assessed (§4.6).

4.1. *System identification based on subspace techniques*

System identification comprises a wide range of methods of varying applicability and complexity (see Ljung (1999)). In our case, we aim at obtaining a linear time-invariant (LTI) multiple-input-multiple-output (MIMO) system, such as the one given in Eq. (3.3). In general, we have $u(n)$ as known inputs, $w(n)$ as unknown white plant noise and $y(n)$ as known outputs corrupted by unknown white noise $v(n)$. We aim at determining the system matrices ($\mathcal{A}, \mathcal{B}, \mathcal{C}$ and $\mathcal{D}$), which govern a state $x(n)$ such that

$$x(n+1) = \mathcal{A}x(n) + \mathcal{B}u(n) + w(n), \tag{4.1a}$$

$$y(n) = \mathcal{C}x(n) + \mathcal{D}u(n) + v(n). \tag{4.1b}$$

The coefficients of the system matrices are chosen such that the estimated output $y_e(n)$, obtained by time-marching (4.1) with $w(n) = v(n) = 0$, is as close as possible to the measured output $y(n)$ (subject to the white-noise sources $w(n)$ and $v(n)$), knowing the inputs $u(n)$. We stress that the state $x(n)$ does not necessarily have to have a physical interpretation.

System identification consists of three procedural steps (see figure 4). First, the system

is excited by known and unknown input signals $u(n)$ and $w(n)$ while the outputs $y(n)$ (corrupted by noise $v(n)$) are recorded. In a second step, a parametrized model is chosen, in our case a LTI system characterized by the system matrices $\mathcal{A}, \mathcal{B}, \mathcal{C}$ and $\mathcal{D}$, together with an appropriate identification algorithm. A subsample of the full data set, referred to as the learning dataset, is then processed to determine the system matrices of the model. In a third step, a different part of the data, known as the testing dataset, is used to drive the identified system, and the output $y_e(t)$ produced by the model is compared to the measured true output $y(t)$; based on this validation test, the model is accepted, adapted or rejected.

The form of the model given in (4.1) makes subspace identification algorithms a convenient choice. Appendix A presents a brief introduction to these techniques; a more comprehensive description is given in Qin (2006) and Van Overschee & De Moor (1996). In this study, the `N4SID` algorithm (Van Overschee & De Moor 1994) has been used to obtain all the models.

4.2. *Outputs as coefficients of velocity snapshots in a POD basis*

We would like to describe the system at each time instant with velocity snapshots $\mathbf{u}_{\text{snap}}$. The large number of degrees of freedom in these snapshots makes direct application of identification techniques excessively, or prohibitively, expensive. It is thus necessary to reduce the dimensionality of the measured data. In this article, we use the proper orthogonal decomposition (POD) modes (Lumley 1967; Sirovich 1987) to form a reduced basis. Note that, contrary to the previous section, the velocity snapshots used to build the POD basis are obtained in the presence of the true, but unknown, noise environment $w(t)$.

We consider a sequence of m velocity snapshots $\{\mathbf{V}_{\text{snap}}(n)\}_{n=1..m}$ extracted from the Ω_{snap}-domain and containing the effect of upstream noise w. The sequence needs to cover a sufficiently large time range to explore all states of the system. Therefore, even though not mandatory, the time-delay between two snapshots can be taken as quite large, so as to obtain nearly uncorrelated successive snapshots. The proper orthogonal decomposition then enables us to compute a ranked orthonormal basis $\{\mathbf{\Phi}_i\}_{i=1..m}$ of flow fields, satisfying $\langle \mathbf{\Phi}_i, \mathbf{\Phi}_j \rangle = \delta_{ij}, \quad i,j = 1,2,...,m$, which can be expressed most conveniently as a linear combination of these m snapshots. Here, the scalar-product $\langle \cdot \rangle$ is associated with the energy-based inner product: $\left\langle \mathbf{u}^1_{\text{snap}}, \mathbf{u}^2_{\text{snap}} \right\rangle = \int_{\Omega_{\text{snap}}} (u^1_{\text{snap}} u^2_{\text{snap}} + v^1_{\text{snap}} v^2_{\text{snap}})\, dx\, dy$. Any velocity field $\mathbf{V}$ in Ω_{snap} can then be projected onto the first k POD modes according to

$$y_i = \langle \mathbf{\Phi}_i, \mathbf{V} \rangle, \qquad i = 1,2,...,k, \tag{4.2a}$$

$$\mathbf{V}' = \sum_{i=1}^{k} \mathbf{\Phi}_i y_i, \tag{4.2b}$$

to produce the approximate flow field $\mathbf{V}'$. Properties of the POD guarantee that, for all k, the error $\|\mathbf{V} - \mathbf{V}'\|^2 = \langle \mathbf{V} - \mathbf{V}', \mathbf{V} - \mathbf{V}' \rangle$ is minimal for the set of m measured snapshots. For the subsequent derivations, we define the reduced state vector given by the k POD coefficients by $\mathbf{Y} = [y_1, y_2, ..., y_k]^T$ and denote the reduced POD basis by $\mathsf{U} = [\mathbf{\Phi}_1, \mathbf{\Phi}_2, ..., \mathbf{\Phi}_k]$.

In what follows, snapshots have been obtained with the smaller Ω_{snap}-domain of dimension $(150, 950) \times (0, 40)$. A total of 1500 snapshots sampled each $\Delta t_{pod} = 5$ have been used to obtain the POD basis. From figure 6 a cut-off for the lower frequencies can be established at $f \approx 10^{-3}$ which, considering the total length T of the time data used to compute the POD basis ($T = 1500 \times 5 = 7500$), guarantees that the lowest physical fre-

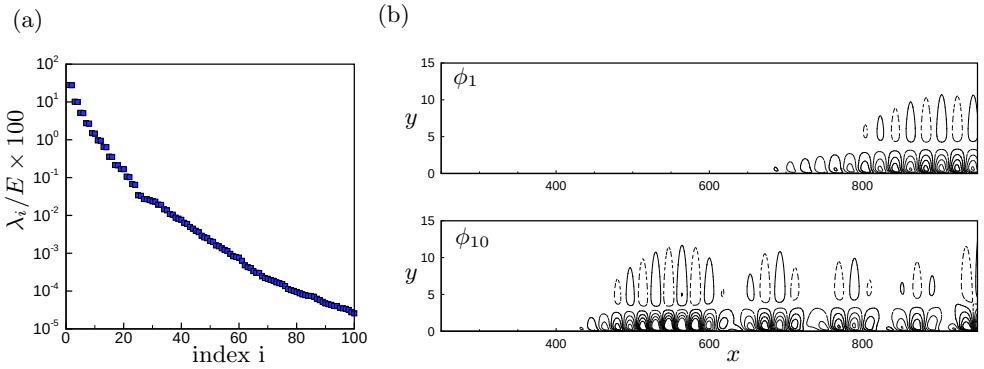

Figure 5: (a) First 100 POD eigenvalues λ_i of the correlation matrix. (b) Contours of the streamwise velocity component of the first ($\mathbf{\Phi}_1$) and tenth ($\mathbf{\Phi}_{10}$) POD-mode.

quencies $f \approx 10^{-3}$ have been explored approximately $7500 \times 10^{-3} \approx 8$ times. Figure 5(a) shows the corresponding eigenvalues of the correlation matrix, confirming a steady decay over about three decades in the first thirty modes (95 % of the energy is contained in the first ten modes). Two selected POD modes, $\mathbf{\Phi}_1$ and $\mathbf{\Phi}_{10}$, are displayed in figure 5(b).

The time-evolving POD coefficients $\mathbf{Y}(n)$ constitute the output of the system. In the next section, we will seek a model structure for a dynamic observer that is able to accurately predict $\mathbf{Y}(n)$ from the input to the system.

4.3. *A dynamic observer obtained by identification techniques*

An approximation $\mathbf{Y}_e$ of the temporal evolution of the reduced state vector $\mathbf{Y}$ can be obtained by time marching a dynamic observer equation, whose structure is similar to the one given in (3.3), that is,

$$\mathbf{Y}_e(n+1) = \widetilde{\mathsf{A}}_s \mathbf{Y}_e(n) + \widetilde{\mathbf{L}} s(n). \tag{4.3}$$

The quantities $\widetilde{\mathsf{A}}_s$, $\widetilde{\mathbf{L}}$ and $\widetilde{\mathbf{C}}$ will be obtained with system identification techniques that solely rely on knowledge of input-output datasets $\{s(n), \mathbf{Y}(n)\}_{n=1..m}$, rather than by performing a Galerkin projection and solving a Riccati equation. A relation between the general formulation of subspace algorithms defined in § 4.1 and the dynamic observer notation can straightforwardly be defined as $\widetilde{\mathsf{A}}_s = \mathcal{C}\mathcal{A}\mathcal{C}^{-1}$ and $\widetilde{\mathbf{L}} = \mathcal{C}\mathcal{B}$, assuming that $\mathcal{D} = 0$.

The input $s(n)$ is related to the state $\mathbf{Y}_e(n)$ according to

$$s(n) = \widetilde{\mathbf{C}} \mathbf{Y}_e(n), \tag{4.4}$$

where $\widetilde{\mathbf{C}}$ is a measurement matrix which can be obtained using two different procedures: its exact definition or an identification techniques. In the first case, we combine equations (2.3) and (4.2) to get

$$\widetilde{\mathbf{C}}_{\mathrm{exact},i} = \int_{x_s}^{x_s+\Delta x} \left. \frac{\partial(\mathbf{\Phi}_i \cdot \tau_x)}{\partial y} \right|_{y=0} dx, \qquad \tau_x = \begin{pmatrix} 1 \\ 0 \end{pmatrix}. \tag{4.5}$$

The evaluation of this expression involves either measuring the POD modes or combining the measurements $\{s(n)\}_{n=1..m}$ associated with the velocity snapshots $\{\mathbf{V}_{\mathrm{snap}}(n)\}_{n=1..m}$, that were used for the construction of the POD basis in §4.2. In the second case, we use a simple least-squares method applied to a composite time-series $\{s(n), \mathbf{Y}(n)\}_{n=1..m}$ of

	Galerkin projection	System identification
Reduced-order state	$\mathbf{X}(n)$	$\mathbf{Y}(n)$
ROM matrices	$\mathsf{A}_w, \mathbf{B}_w$	$\widetilde{\mathsf{A}}_w, \widetilde{\mathbf{B}}_w$
Estimated state	$\mathbf{X}_e(n)$	$\mathbf{Y}_e(n)$
Observer matrices	$\mathsf{A}_s, \mathbf{L}$	$\widetilde{\mathsf{A}}_s, \widetilde{\mathbf{L}}$
Measurement matrix	$\mathbf{C}$	$\widetilde{\mathbf{C}}_{\text{exact}}$ (obtained by definition) $\widetilde{\mathbf{C}}$ (obtained by least-squares)

Table 1: Notation used for the Galerkin-projection- and identification-based design of a dynamic observer.

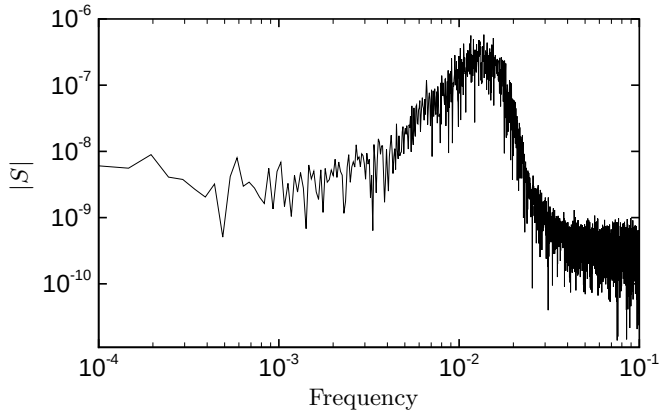

Figure 6: Spectrum of the input signal $s(t)$ obtained from the shear-stress sensor placed at $x = 200$.

the learning dataset. It is straightforward to show that

$$\widetilde{\mathbf{C}} = [s(1) \cdots s(m)][\mathbf{Y}(1) \cdots \mathbf{Y}(m)]^{\dagger}, \tag{4.6}$$

where † denotes the Moore-Penrose pseudo-inverse.

As shown in §3.1, the true evolution matrix for $\mathbf{Y}$ is not $\widetilde{\mathsf{A}}_s$ but $\widetilde{\mathsf{A}}_w$. Considering a model-structure for $\mathbf{Y}$ similar to the one obtained by Gakerkin projection in (3.2), we see that the state $\mathbf{Y}(n)$ is governed by

$$\mathbf{Y}(n+1) = \widetilde{\mathsf{A}}_w \mathbf{Y}(n) + \widetilde{\mathbf{B}}_w w(n), \tag{4.7a}$$

$$s(n) = \widetilde{\mathbf{C}} \mathbf{Y}(n) + g(n), \tag{4.7b}$$

where the known input $\widetilde{\mathbf{L}} s(n)$ has been replaced by the unknown driving term $\widetilde{\mathbf{B}}_w w(n)$. The true evolution matrix $\widetilde{\mathsf{A}}_w$ in (4.7) can thus be obtained from the observer matrix $\widetilde{\mathsf{A}}_s$ via

$$\widetilde{\mathsf{A}}_w = \widetilde{\mathsf{A}}_s + \widetilde{\mathbf{L}}\widetilde{\mathbf{C}}. \tag{4.8}$$

The different notations used for the models obtained with Galerkin projection and identification techniques are summarized in table 1.

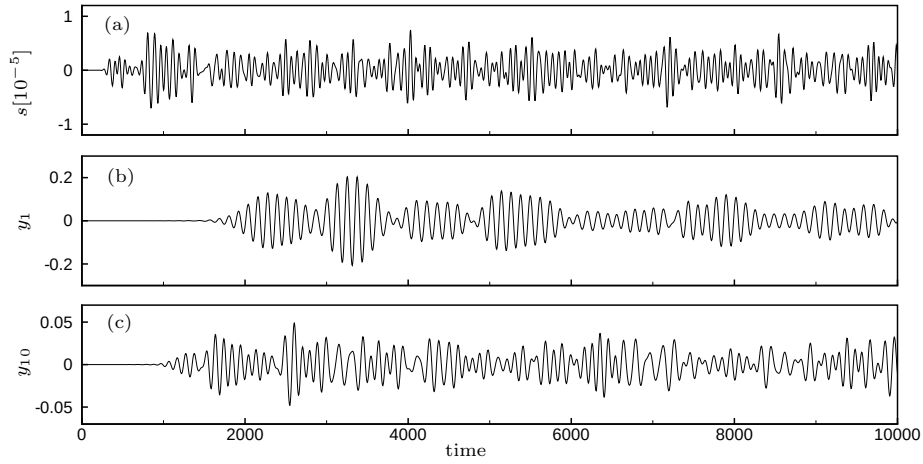

Figure 7: Learning dataset: (a) the measurement s capturing the influence of external noise and (b) and (c) the POD coefficients y_i obtained by projecting the flow field onto the POD modes $\mathbf{\Phi_1}$ and $\mathbf{\Phi}_{10}$, respectively.

4.4. *Identification of model coefficients with learning dataset*

We obtain data by performing a linearized direct numerical simulation of the boundary layer in the presence of unknown noise. We use a sampling interval $\Delta t = 5$ for the velocity snapshots and the shear-stress measurements s. This choice of sampling interval can be justified by regarding figure 6, where the frequency spectrum of the input signal $S(f)$ is represented. This figure shows that the frequency content of s is rather low near the Nyquist frequency $f_{\text{nyquist}} = f_s/2 = 0.1$ defined by our sampling interval $\Delta t = 1/f_s$. The datasets to be processed are composed of the input signal from the sensor s and several outputs y_i corresponding to the projection of the snapshots onto the set of POD modes $\{\mathbf{\Phi}_i\}$ (figure 7). Using the `N4SID` algorithm (Van Overschee & De Moor 1994) and the Moore-Penrose pseuso-inverse, the model parameters $\widetilde{\mathsf{A}}_s$, $\widetilde{\mathbf{L}}$ and $\widetilde{\mathbf{C}}$ are then determined by fitting the model output to the true, measured output, as the model is forced by the recorded input. A reduced-order model has been determined with $k = 90$ POD modes and a learning data set of length $N_{\text{snap}} = 2000$.

4.5. *Assessment of model performance with testing dataset*

The validity of the identified parameters is subsequently confirmed by using a *different* data set (referred to as the testing data set) and by comparing the model output to the true output. As this testing data set has not been used in the identification of the model, we can assess the predictive capability of the identified model in this manner. The kinetic energy defined as $E(t) = \langle \mathbf{u}_{\text{snap}}, \mathbf{u}_{\text{snap}} \rangle \approx \mathbf{Y}^*\mathbf{Y}$ is an important variable of the system since it represents the global dynamics of the flow. The quality of fit between the energy of the DNS, denoted by $E(t)$, and the value predicted by the model, denoted by $\widetilde{E}(t)$, can be stated as

$$\mathsf{FIT}[\%] = 100 \left(1 - \frac{\left\| E(t) - \widetilde{E}(t) \right\|}{\| E(t) - \text{mean}(E(t)) \|} \right) \tag{4.9}$$

and can be used to quantify the performance of the estimator. Figure 8(a) displays the measured input signal s from the wall shear-stress sensor, from which all subsequent flow variables (figure 8(b-e)) can be derived using the identified model. In our case,

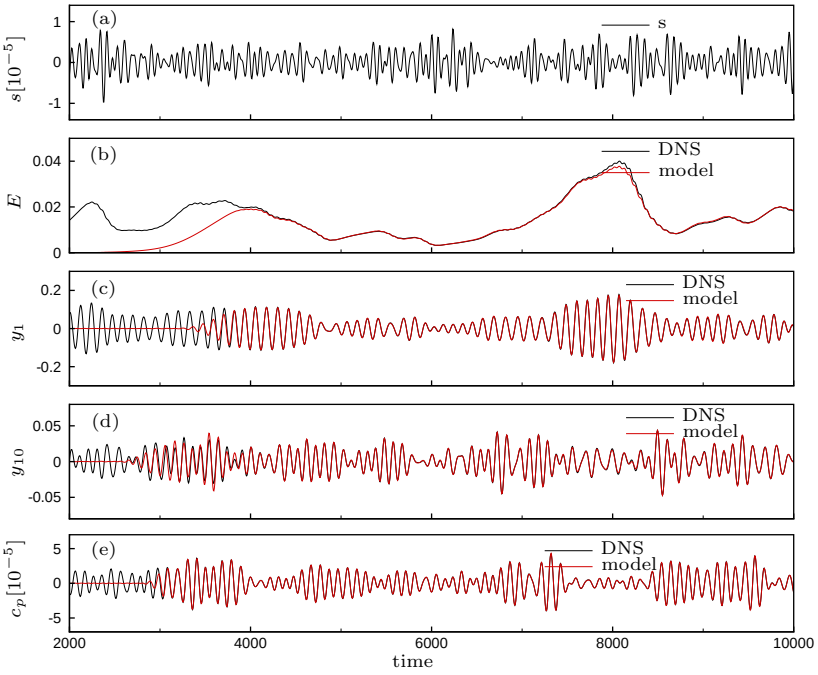

Figure 8: Validation dataset: performance of the system-identified model, initialized by $\mathbf{Y} = 0$ at $t = 2000$. The input data from the wall shear-stress sensor s is shown in (a); the remaining flow variables are recovered solely from this measurement signal using the identified model. (b-e) Comparison between the DNS (black) and the model prediction (red) for four variables from the testing dataset: (b) the energy of the system, (c) and (d) the POD coefficients y_i for the first and tenth modes, respectively, and (e) a friction sensor c_p placed at $x = 600$.

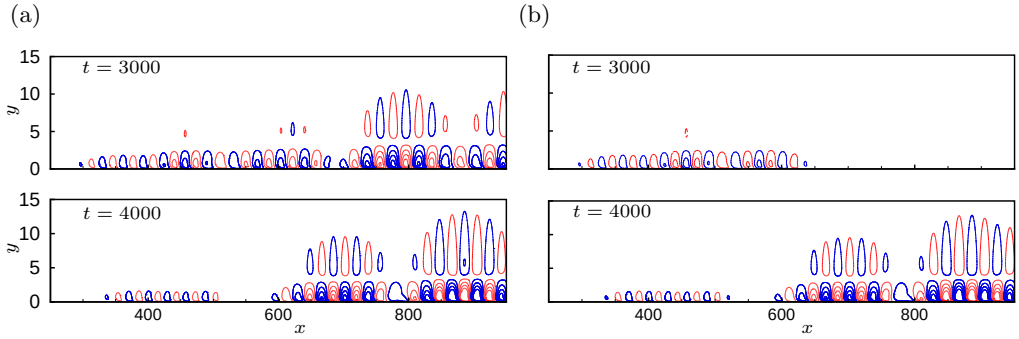

Figure 9: Snapshots of the streamwise disturbance velocity component obtained (a) from the DNS and (b) recovered from $s(n)$ via the model for $t = 3000$ and $t = 4000$. See supplementary movie 1.

we show the evolution of energy (b), the first and tenth POD coefficient (c,d) and the output from a friction sensor (e) placed at $x = 600$. After a short transient period, the predicted flow variables closely track their true DNS-equivalents, which yields a relative match of $\mathsf{FIT}_{\text{ener}} = 93.72\%$ when evaluated over the time interval $t \in [4000, 10000]$. The length of the transient period, estimated as $T_{\text{trans}} \approx 2000$, can be directly linked to the

convective time of the disturbances. As previously mentioned, Tollmien-Schlichting waves are convected with a group velocity equal to $v_g = 0.375$. This convective velocity defines the characteristic time T_{conv} necessary for the wavepacket to cover the distance between the sensor s and the downstream edge of the domain Ω_{snap}. This time ($T_{\text{conv}} \approx 2000$) accurately predicts the duration of transient effects T_{trans}. This match between the time the estimator needs to propagate information and the time the system needs to convect a wavepacket confirms that the input-output behavior of the system is well-captured by the model. From the POD coefficients in $\mathbf{Y}_e$ the full flow field can be reconstructed from the basis U. Two examples of this reconstruction, visualized by the streamwise velocity component, are shown in figure 9 and compared to the equivalent full DNS simulation. The first instant at $t = 3000$ has been taken during the transient phase and shows a promising but incomplete match over the entire flow domain; a second instant at $t = 4000$ displays an excellent agreement between the flow structure recovered from $s(t)$ via the identified model and the full DNS solution.

4.6. *Influence of some model parameters on performance*

System-identification techniques usually contain numerous model parameters which have to be determined with care in order to obtain a representative and robust model of the underlying physical process. Subspace identification methods are particularly advantageous in this respect, when compared to parametrized models (see Hervé *et al.* (2012)), due to the relative simplicity of their parametrization; in fact, the size of the state-space model is the only user-defined parameter for subspace techniques.

In this section, we study the influence of the state-space size k (in other words, the number of POD modes), as well as the number of snapshots N_{snap} contained in the learning dataset, on the quality of our identified reduced-order model. Figure 10 represents the statistical mean and standard deviation of the fit between the validation dataset and the predictions of different models. Both graphs have been obtained by computing, for each point on the curves, ten models obtained from distinct sections of a long learning dataset. The total length of the learning dataset is $N_{\text{snap}} = 8000$ (40000 time units) and the different learning sections i begin at different time instants, $t^{\text{init}}_{i=0..9} = 2500+500i$. Figure 10(a) shows, for a fixed number of POD modes ($k = 90$), the influence of the number of snapshots N_{snap}: we observe that a minimum number of snapshots are necessary to obtain an accurate model. This observation is common in identification techniques, since the algorithm requires sufficiently long time sequences from the dynamical system to arrive at statistically converged data. In our case, the identification procedure requires about $1500 \times 5 = 7500$ characteristic time units to obtain satisfactory results (signal components of the lowest system frequency $f = 10^{-3}$ have been explored about 8 times).

The influence of the number of POD modes k on the model quality (fit) observed in Figure 10(b) is far less trivial. For a fixed number of snapshots $N_{\text{snap}} = 2000$, a minimum number of $k = 40 - 50$ POD modes are required to obtain a good performance of the dynamic observer: this is related to the concept of observability of the POD basis.

Intuitively, a necessary condition for an observable system requires that the input $s(n)$ and the state $\mathbf{Y}(n)$ are well correlated or, in other words, that the measurement $s(n)$ must be accurately representable by the POD coefficients according to $s(n) \approx \widetilde{\mathbf{C}}\mathbf{Y}(n)$. Figure 11 shows the relative error between the measurement $s(n)$ given by the sensor in the DNS simulation and the measurement $s = \widetilde{\mathbf{C}}\mathbf{Y}$, with $\mathbf{Y}$ obtained by projection of the velocity snapshots onto the POD modes. The solid and dashed lines respectively represent the relative error for the case where $\widetilde{\mathbf{C}}$ is obtained by measuring the POD modes (Eq. (4.5)) and by the pseudo-inverse (Eq. (4.6)). Both curves show a similar behavior, reflecting the fact that, after a minimum number of POD modes are taken into

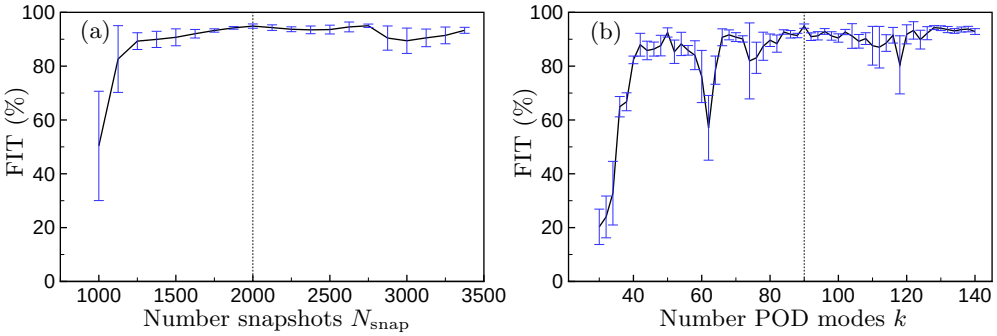

Figure 10: Influence of the model parameters on the quality of the identification. Mean (black) and standard deviation (blue) of the validation fit computed from samples of ten models obtained from different learning datasets. (a) Influence of the length of the learning dataset N_{snap} (for a fixed number of POD modes $N_{\text{pod}} = 90$) and (b) of the number of POD modes k (for a fixed number of snapshots $N_{\text{snap}} = 2000$).

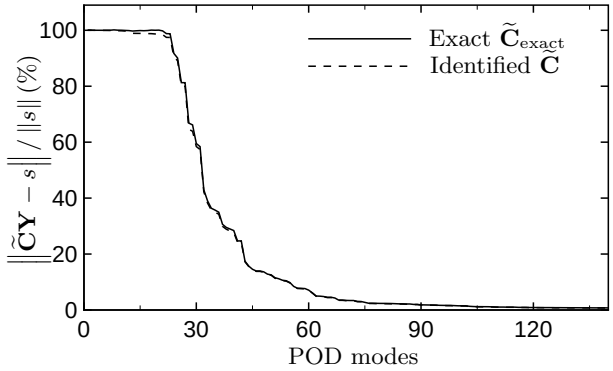

Figure 11: Relative error between the signal $s(t)$ obtained by DNS and the signal given by $\widetilde{\mathbf{C}}_{\text{exact}}\mathbf{Y}(t)$ (exact definition) and $\widetilde{\mathbf{C}}\mathbf{Y}(t)$ (estimated by least-squares) for different numbers of POD modes. $\|\cdot\|$ indicates the 2-norm on the vertical axis.

account, the POD basis accurately captures the temporal behavior of the measurement signal $s(n)$. The relatively high degree of the system ($N_{\text{pod}} = k = 90$) is related to the inherent lack of observability of the POD basis. Proper orthogonal decomposition maximizes the energy captured by a few orthogonal modes and, as is the case for the boundary layers (and, more generally, flow amplifiers), the most energetic structures are commonly localized downstream in the domain of interest. Consequently, the first POD modes do not show much spatial support in the upstream part of the domain, and higher modes are necessary to represent the full dynamics of $s(n)$. Figure 12 demonstrates this tendency, showing that the energy content of the modes at the location of the estimation sensor is nearly zero up to the 22^{nd} POD-mode.

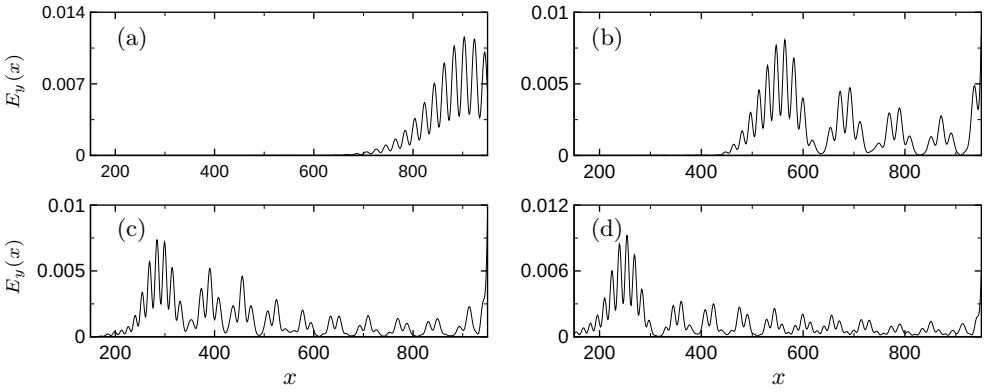

Figure 12: Local kinetic energy $E_y(x) = \int_0^\infty (u^2 + v^2) dy$ for four POD modes: (a) $\mathbf{\Phi}_1$, (b) $\mathbf{\Phi}_{10}$, (c) $\mathbf{\Phi}_{22}$ and (d) $\mathbf{\Phi}_{24}$. The estimation sensor is located at $x_s = 200$.

5. Comparison of model obtained by system identification with other techniques

In this section, we compare the performance of our identified dynamic observer to that of a more common Galerkin-based observer (§5.1) and to that of a Linear-Stochastic-Estimation (LSE)-based observer (§5.2).

5.1. *Comparison with model obtained by Galerkin projection*

The identification-based dynamic observer presented in this article is similar to the one obtained by Galerkin projection. However, the identification process will introduce a bias in the obtained model; this bias will be analyzed below. In figure 13, we compare the performances of the dynamic observer established in (3.3) by Galerkin projection and the one obtained in (4.3) by identification methods. Even though the temporal evolution of the POD coefficients is quite similar in both models, a slight overestimation in energy is observed in the identified system. The temporal evolution of the POD coefficients furthermore shows small oscillations in the signal of the identified model (noticeable for sufficiently small signal amplitudes; see $3000 < t < 4000$ in figures 13(a,b)). This oscillatory effect often appears in identified models and stems from an inadequate representation of some frequencies. It is important, however, to keep in mind that both models are associated with slightly different bases, but a fair comparison has to be performed on a common basis. To this end, we have chosen to project the estimated state $\mathbf{X}_e$ onto the POD basis U used to obtain the identified model.

5.2. *Comparison with model obtained by LSE*

Linear stochastic estimation (LSE) postulates a static linear relationship between a set of input signals (measurements from sensors) and a set of output variables of the flow. The LSE estimator can be formulated as

$$\mathbf{Y}_e(n) = \widetilde{\mathsf{R}}\mathbf{S}(n), \tag{5.1}$$

where $\mathbf{Y}_e(n) \in \mathbb{R}^k$ and $\mathbf{S}(n) \in \mathbb{R}^m$ are vectors containing, respectively, the k estimated output variables by LSE at time n and the measurements from m sensors at time n, and $\widetilde{\mathsf{R}}$ is a matrix obtained by minimizing the mean-squared error between the true output and the one predicted by the model, in other words, $\|\mathbf{Y} - \mathbf{Y}_e\|^2$.

In our numerical experiments, a linear estimator has been computed based on input from ten shear-stress sensors (equispaced between $x = 500$ to $x = 950$) and 20 POD

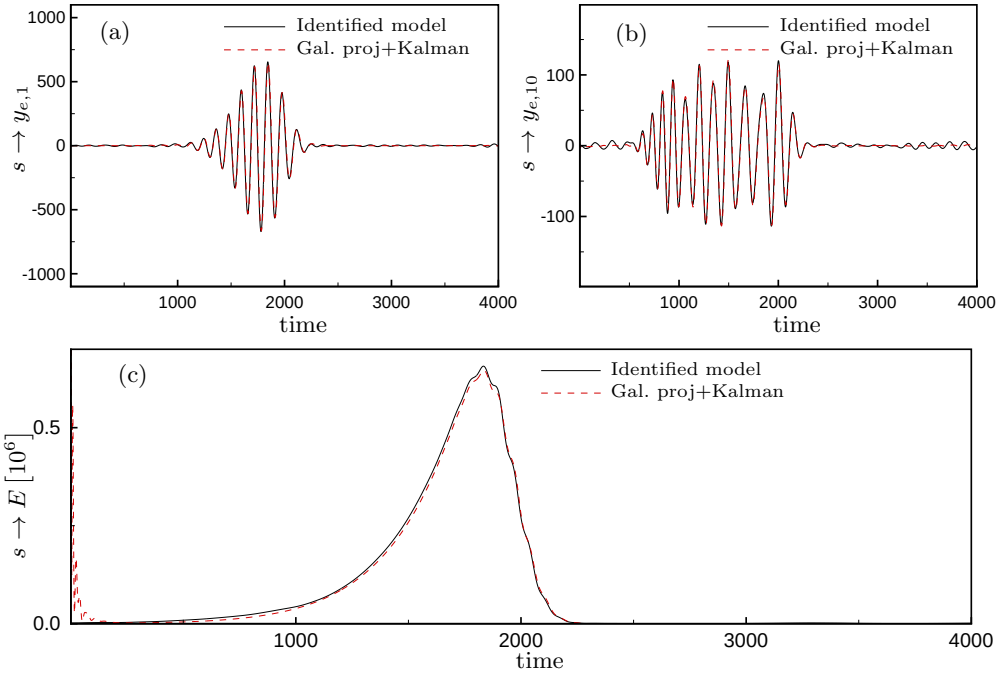

Figure 13: Galerkin-based ROM vs. estimated model impulse responses. (a) from s to $y_{e,1}$, (b) from s to $y_{e,10}$ and (c) from s to the perturbation energy $E = \mathbf{Y}_e^* \mathbf{Y}_e$.

modes representing the flow state. Figure 14 shows a comparison of DNS results with results obtained from applying either LSE or a dynamic observer. It appears that, in the case of LSE, a great many more sensors are required to obtain a model of similar quality (performance) than the one provided by the dynamic observer. This observation corroborates the need of the estimator to correctly identify the wavelengths of the Tollmien-Schlichting waves – a requirement that can be met with very closely spaced sensors. By comparing different POD coefficients, this point can be further substantiated. For instance, in figure 14, the first POD coefficient y_1 (corresponding to a structure with large wavelengths) is well represented by the model, while the tenth and twentieth POD coefficients (y_{10} and y_{20}), associated with far shorter wavelengths, deviate more noticeably from the DNS results. Moreover, the energy predicted by the LSE-model appears rather noisy compared to the DNS. This feature arises, again, from the poor representation of the shorter wavelengths of the flow, but it also stems from the inherent lack of accuracy of first-order truncated stochastic models. This second source of inaccuracies can be alleviated by considering higher-order terms, while adding closer-spaced sensors will achieve a better representation of the poorly estimated wavelengths. It is also important to notice that the linear stochastic estimator does not contain a transient phase, as the dynamic observer does. Furthermore, it needs fewer POD modes: the dynamic observer requires a large number of POD modes to fulfill the observability condition discussed in §4.6, whereas the linear stochastic estimator is not subjected to this constraint. It has been verified that including more than 20 POD modes does not further improve the performance of the LSE model.

Figure 15 represents snapshots of the streamwise disturbance velocity at a given instant ($t = 8000$) for six different cases. The first two snapshots represent results from

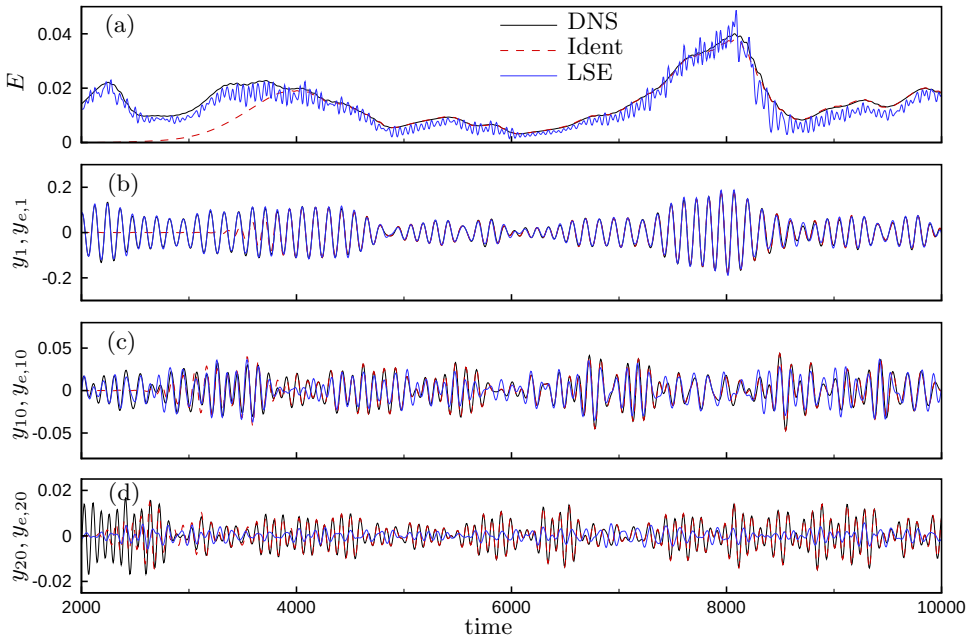

Figure 14: Performance of LSE compared to the dynamic observer. The input data used by the LSE model comes from ten equispaced shear-stress sensors between $x = 500$ to $x = 950$, while the dynamic observer uses a single sensor located at $x_s = 200$. (a-d) Comparison between the linearized DNS (black), the identified dynamic observer prediction (red dashed) and the LSE model (blue) for three variables from the testing dataset: (a) the energy of the system and (b-d) the POD coefficients y_i for the first, tenth and twentieth mode, respectively.

the DNS and from a reconstruction by the identified dynamic observer based on a single sensor located at $x_s = 200$, respectively. The last four snapshots are obtained via LSE using different numbers of sensors placed at different positions. In the first of the LSE-cases (figure 15(c)), seventeen equispaced sensors, located between $x = 150$ and $x = 950$, are considered. A satisfactory prediction of the velocity field is obtained with this configuration, even though the structures far upstream are not as well represented when compared to the dynamic observer. In figures 15(d,e) ten sensors have been placed equidistantly, in one case, between $x = 500$ and $x = 950$ and, in a second case, between $x = 150$ and $x = 600$. When the ten sensors are concentrated in the downstream part of the domain, upstream information is lost and vice versa for an upstream placement of the sensors. Finally, figure 15(f) uses only two sensors (at $x = 200$ and $x = 950$): this time, LSE fails to recover any relevant information about the flow structures. These results underline the fact that linear stochastic estimation requires spatial support of the input information (sensors) over the whole domain due to the strong convection, while the dynamic observer only needs information from a localized input signal. In summary, the above numerical experiments show that a dynamic observer model is preferable over a linear stochastic estimator (LSE) model in providing an accurate approximation of the flow field from localized and sparse measurements.

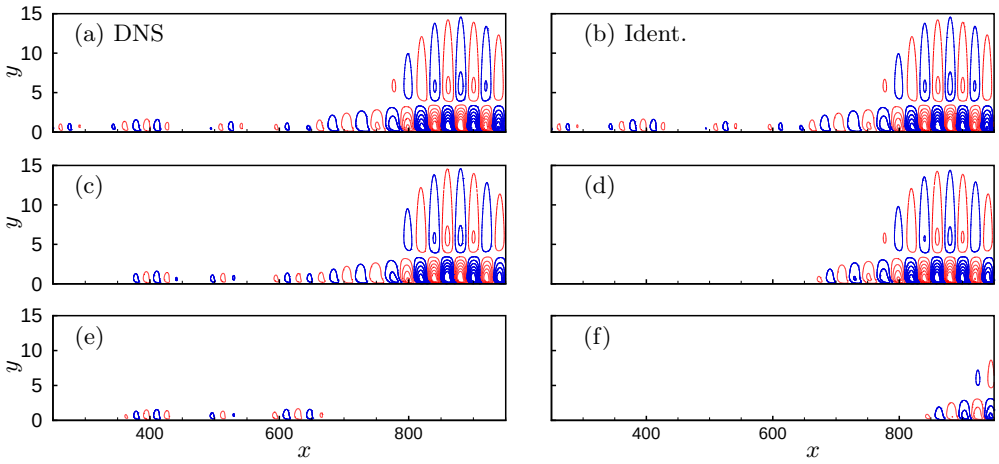

Figure 15: Snapshots of the streamwise disturbance velocity at $t = 8000$ obtained (a) from linearized direct numerical simulations (DNS), (b) recovered from a single sensor via the identified dynamic observer, (c-f) recovered from shear-stress sensors via a LSE model: (c) from seventeen sensors equispaced between $x = 150$ to $x = 950$, (d) from ten sensors equispaced between $x = 500$ to $x = 950$, (e) from ten sensors sensors equispaced between $x = 150$ to $x = 600$ and (f) from two sensors placed at $x = 150$ and $x = 950$.

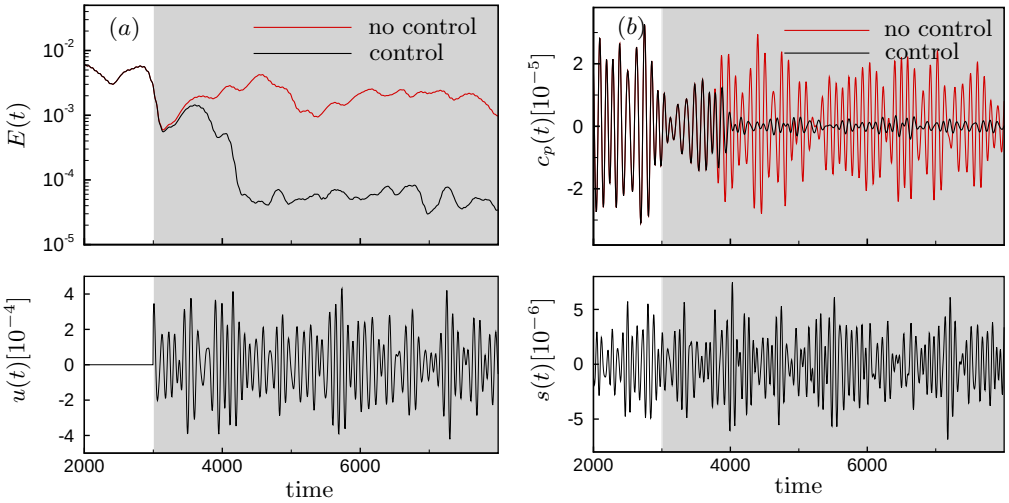

Figure 16: Results of the LQR-control design based on the dynamic observer. (a) Temporal evolution of the perturbation energy $E(t)$ for the uncontrolled simulation (red) and the controlled simulation targeting the energy (black), together with the control signal $u(t)$ obtained in the case of the energy objective (see supplementary movie 2). (b) Time signal of the friction sensor $c_p(t)$ placed at $(x_{c_p}, y_{c_p}) = (600, 0)$ for the uncontrolled (red) and controlled simulation targeting the sensor signal c_p (black), together with the sensor signal s, which is the same in all simulations discussed in this figure.

6. Application of optimal control

The successful recovery of full-state information from single wall shear-stress measurements by a dynamic observer enables the design of a variety of effective control schemes, which we demonstrate next. For this purpose, a control signal u is placed at $(x_u, y_u) = (250, 1)$ (downstream of the sensor s), which constitutes a feedforward control configuration. The governing equations (3.3) of the dynamic observer are modified to reflect this addition. We have

$$\mathbf{Y}_e(n+1) = \widetilde{\mathsf{A}}_s \mathbf{Y}_e(n) + \widetilde{\mathbf{L}} s(n) + \widetilde{\mathbf{B}}_u u(n). \tag{6.1}$$

Following Hervé *et al.* (2012), the system is excited with a frequency-rich signal u in order to identify the new term $\widetilde{\mathbf{B}}_u$. The unknown system matrices $\widetilde{\mathsf{A}}_s$, $\widetilde{\mathbf{L}}$ and $\widetilde{\mathbf{B}}_u$ may then be determined in a similar way as described in § 4. From there, the true linear system matrix $\widetilde{\mathsf{A}}_w$ which governs the perturbation dynamics ((4.7) with added control term) can be extracted following (4.8). This matrix is then used for the design of an LQR-optimal controller $u(n) = \mathbf{K}\mathbf{Y}(n)$, which minimizes the cost functional $\sum_{n=0}^{\infty} \mathbf{Y}(n)^* \mathsf{Q} \mathbf{Y}(n) + \ell^2 |u(n)|^2$, where Q is a positive definite weight matrix and ℓ is a user-specified parameter to balance disturbance energy and exerted control energy. Following standard procedure (see Burl (1999)), the control gain $\mathbf{K}$ can be obtained by solving a Riccati equation involving $\widetilde{\mathsf{A}}_w$, $\widetilde{\mathbf{B}}_u$, Q and ℓ.

Two different control objectives Q have been considered: (i) the suppression of the energy $E(t)$ inside the velocity window ($\mathsf{Q} = \mathsf{I}$) and (ii) the control of the signal variance recorded by the downstream friction-sensor c_p ($\mathsf{Q} = \widetilde{\mathbf{C}}_p^* \widetilde{\mathbf{C}}_p$, with $\widetilde{\mathbf{C}}_p$ as the measurement vector associated with c_p and obtained with the least-squares technique introduced in § 4.3 to obtain $\widetilde{\mathbf{C}}_s$). We use a model that comprises 50 modes computed on a shorter domain ($\Omega_{\text{snap}} = (200, 700) \times (0, 40)$). In the controlled simulation, the measurement s is used to reconstruct the full perturbation field $\mathbf{Y}_e$ based on the identified model, and the control law is obtained by applying the control gain $\mathbf{K}$ to this state. Results are shown in figure 16 together with the control signal $u(t)$ and the friction-sensor signal s. In both cases, a substantial reduction in the respective objectives can be accomplished. The energy $E(t)$ has been reduced by nearly two orders of magnitude (a reduction of 96.81% in the mean perturbation energy), while the rms-value of the friction sensor signal has been lowered by about 88.01%.

7. Summary and conclusions

A dynamic observer recovering full-state information from single wall shear-stress measurements has been designed that relies on a POD basis (from measured snapshots) and system identification techniques. For noise-amplifier flows, it successfully reproduces the perturbation dynamics (velocity fields) throughout the full sampling domain and furnishes information about the flow that can subsequently be used by itself, for flow diagnostics or, in a second step, for LQR-control design.

Within the limits of linear perturbation dynamics, the design process for the dynamic observer extracts the system matrix from a sequence of snapshots; this system matrix describes a globally stable flow configuration that is sustained by selectively amplified random perturbations from the noise environment. The proposed method thus successfully separates the intrinsic, stable perturbation dynamics from the external noise excitation, which previously could only be quantified in its entirety.

A wide variety of flow analyses is possible once the system matrix has been extracted. In the present case, we chose to design a closed-loop control scheme which, owing to the

known system matrix, could now be accomplished using full-state information control (LQR) algorithms. As a consequence, a significant reduction of the perturbation energy or sensor signal rms-values could be achieved. Even though system identification could have been used to determine a direct input-to-output control law targeting the variance of a downstream wall-sensor (Hervé *et al.* 2012), the retrieval of full-state information gives a far more physical and structural view of dynamic processes.

The input data for the design procedure of the dynamic observer are readily available in experiments, and an application of a dynamic observer in a suitable experiment is currently planned and will be explored in a future effort. However, difficulties not accounted for in the present paper are expected to arise in an experimental situation: noise corrupting the PIV and friction measurements, the presence of non-localized external forcing or the presence of non-linearities are some examples. These challenges will be addressed in a forthcoming study.

Acknoledgements

The authors would like to thank J.C. Robinet and A. Hervé for fruitful conversations, as well as J.C. Loiseau for his support with `Nek-5000`.

Appendix A. Subspace identification algorithms

Subspace identification algorithms consider the state-space formulation of a stochastic linear system. Such a system can be written in the following *process form*

$$x(n+1) = \mathcal{A}x(n) + \mathcal{B}u(n) + w(n) \tag{A 1a}$$

$$y(n) = \mathcal{C}x(n) + \mathcal{D}u(n) + v(n) \tag{A 1b}$$

where $y(n) \in \mathbb{R}^{n_y}$, $x(n) \in \mathbb{R}^n$, $u(n) \in \mathbb{R}^{n_u}$, $w(n) \in \mathbb{R}^n$, $v(n) \in \mathbb{R}^{n_y}$ are the system output, state, input, state noise, and output measurement noise, respectively. The matrices $\mathcal{A}$, $\mathcal{B}$, $\mathcal{C}$ and $\mathcal{D}$ are system matrices of appropiate dimensions. The noise covariances of the system are defined as

$$\mathcal{E}\left\{ \begin{pmatrix} w_j \\ v_j \end{pmatrix} \begin{pmatrix} w_i \\ v_i \end{pmatrix}^T \right\} = \begin{pmatrix} \mathcal{Q} & \mathcal{S} \\ \mathcal{S}^T & \mathcal{R} \end{pmatrix} \delta_{ij} \tag{A 2}$$

where $\mathcal{E}\{x\}$ stands for the expected-value operator.

The general problem of subspace identification consists of obtaining the system matrices $\mathcal{A}$, $\mathcal{B}$, $\mathcal{C}$ and $\mathcal{D}$, as well as the covariance matrices $\mathcal{Q}$, $\mathcal{S}$, and $\mathcal{R}$, from observing a set of input-output measurements.

A.1. *Reformulation of the state-space system*

The state-space system (A 1) can be rearranged into two equivalent formulations that emphasize either prediction or estimation (Qin 2006). Considering either formulation, the one-step linear equations can be written as a multi-step matrix-based expression which will form the foundation of subspace system-identification techniques.

Assuming that the system is observable, a Kalman filter can be designed to estimate the state variable. We have

$$\widehat{x}(n+1) = \mathcal{A}\widehat{x}(n) + \mathcal{B}u(n) + \mathcal{K}\left[y(n) - \mathcal{C}\widehat{x}(n) - \mathcal{D}u(n)\right] \tag{A 3}$$

which (omitting the $\widehat{\ }$) leads to the following *innovation form*

$$x(n+1) = \mathcal{A}x(n) + \mathcal{B}u(n) + \mathcal{L}e(n) \tag{A 4a}$$

$$y(n) = \mathcal{C}x(n) + \mathcal{D}u(n) + e(n) \tag{A 4b}$$

where $\mathcal{L}$ is the Kalman gain (which can be obtained from a Riccati equation) and $e(n) = y(n) - \mathcal{C}\widehat{x}(n) - \mathcal{D}u(n)$ is the measurement error.

A third equivalent representation, the *predictor form*, can be written as follows

$$x(n+1) = \mathcal{A}_e x(n) + \mathcal{B}_e \mathbf{z}(n) \tag{A 5a}$$

$$y(n) = \mathcal{C}x(n) + \mathcal{D}u(n) + e(k) \tag{A 5b}$$

where $\mathbf{z}(n) = \left[u^T(n), y^T(n)\right]^T$, $\mathcal{A}_e = \mathcal{A} - \mathcal{L}\mathcal{C}$, and $\mathcal{B}_e = [\mathcal{B} - \mathcal{L}\mathcal{D}, \mathcal{L}]$. It should be stressed again that the three model forms can represent the input and ouput data $(u(n), y(n))$ exactly. We thus have the choice of using any of these models according to convenience.

As a next step, the above one-step vector-based linear difference equations are recast into multi-step matrix-based expressions. We first define an extended state sequence $\mathbf{X}(n) = \big(x(n), \quad x(n+1), \quad \ldots, \quad x(n+N-1)\big)$ which contains N columns describing the state at N consecutive time steps. By iterating p times the predictor form (A 5) it is straightforward to derive the following extended equation,

$$\mathbf{X}(n) = \mathcal{L}_p \mathbf{Z}_p + \mathcal{A}_e^p \mathbf{X}(n-p) \tag{A 6}$$

where

$$\mathcal{L}_p = \left(\mathcal{B}_e, \quad \mathcal{A}_e\mathcal{B}_e, \quad \ldots, \quad \mathcal{A}_e^{p-1}\mathcal{B}_e\right), \tag{A 7a}$$

$$\mathbf{Z}_p = \begin{pmatrix} \mathbf{z}(n-1) & \mathbf{z}(n) & \ldots & \mathbf{z}(n+N-2) \\ \mathbf{z}(n-2) & \mathbf{z}(n-1) & \ldots & \mathbf{z}(n+N-3) \\ \vdots & \vdots & \ddots & \vdots \\ \mathbf{z}(n-p) & \mathbf{z}(n-p+1) & \ldots & \mathbf{z}(n-p+N-1) \end{pmatrix}. \tag{A 7b}$$

Under the assumption that all eigenvalues of the estimator matrix $\mathcal{A}_e$ fall strictly inside the unit circle and in the limit $p \to \infty$, the term $\mathcal{A}_e^p$ can be neglected. This result can be proven valid even for finite p (Van Overschee & De Moor (1994), Van Overschee & De Moor (1996)). Equation (A 6) can then be simplified to

$$\mathbf{X}(n) = \mathcal{L}_p \mathbf{Z}_p. \tag{A 8}$$

In addition, if a similar recursive iteration technique is applied to the innovation form (A 4) we obtain

$$\mathbf{Y}_f = \mathcal{O}_f \mathbf{X}(n) + \mathcal{H}_f \mathbf{U}_f + \mathcal{G}_f \mathbf{E}_f \tag{A 9}$$

where the subscript $_f$ denotes the future horizon. Next, the input, output and innovation data are arranged into Hankel matrices, denoted respectively by $\mathbf{U}_f$, $\mathbf{Y}_f$ and $\mathbf{E}_f$. The structure of these matrices is as follows

$$\mathbf{U}_f = \begin{pmatrix} u(n) & u(n+1) & \ldots & u(n+N-1) \\ u(n+1) & u(n+2) & \ldots & u(n+N) \\ \vdots & \vdots & \ddots & \vdots \\ u(n+f-1) & u(n+f) & \ldots & u(n+f+N-2) \end{pmatrix}, \tag{A 10}$$

and similar for $\mathbf{Y}_f$ and $\mathbf{E}_f$.

Furthermore, $\mathcal{O}_f$ is the extended observability matrix, and $\mathcal{H}_f$, $\mathcal{G}_f$ are Toeplitz matrices of the form

$$\mathcal{O}_f = \begin{pmatrix} \mathcal{C} \\ \mathcal{C}\mathcal{A} \\ \vdots \\ \mathcal{C}\mathcal{A}^{f-1} \end{pmatrix}, \tag{A 11a}$$

$$\mathcal{H}_f = \begin{pmatrix} \mathcal{D} & 0 & \dots & 0 \\ \mathcal{C}\mathcal{B} & \mathcal{D} & \dots & 0 \\ \vdots & \vdots & \ddots & \vdots \\ \mathcal{C}\mathcal{A}^{f-2}\mathcal{B} & \mathcal{C}\mathcal{A}^{f-3}\mathcal{B} & \dots & \mathcal{D} \end{pmatrix}, \tag{A 11b}$$

$$\mathcal{G}_f = \begin{pmatrix} \mathcal{I} & 0 & \dots & 0 \\ \mathcal{C}\mathcal{K} & \mathcal{I} & \dots & 0 \\ \vdots & \vdots & \ddots & \vdots \\ \mathcal{C}\mathcal{A}^{f-2}\mathcal{K} & \mathcal{C}\mathcal{A}^{f-3}\mathcal{K} & \dots & \mathcal{I} \end{pmatrix}. \tag{A 11c}$$

Combining (A 8) and (A 9) we obtain

$$\mathbf{Y}_f = \mathcal{H}_{fp}\mathbf{Z}_p + \mathcal{H}_f\mathbf{U}_f + \mathcal{G}_f\mathbf{E}_f \tag{A 12}$$

where $\mathcal{H}_{fp} = \mathcal{O}_f\mathcal{L}_p$ is the product of the process observability matrix and the predictor controllability matrix. Equation (A 12) plays an essential role in subspace identification algorithms.

A.2. *Extraction of the observability matrix $\mathcal{O}_f$*

The goal of the subsequent steps is to recover the matrix $\mathcal{H}_{fp}\mathbf{Z}_p$, and then $\mathcal{O}_f$ from it. First, $\mathbf{U}_f$ is eliminated from equation (A 12) by post-multiplying by the projection onto its orthogonal complement $\mathcal{P}^{\perp}_{U_f} = \mathcal{I} - \mathbf{U}_f^T(\mathbf{U}_f\mathbf{U}_f^T)^{-1}\mathbf{U}_f$. In addition, if we assume that the innovation sequence $e(n)$ is composed of a stationary, white noise completely uncorrelated with the input $u(n)$ we have $\mathbf{E}_f\mathcal{P}^{\perp}_{U_f} = \mathbf{E}_f$ which yields

$$\mathbf{Y}_f\mathcal{P}^{\perp}_{U_f} = \mathcal{H}_{fp}\mathbf{Z}_p\mathcal{P}^{\perp}_{U_f} + \mathcal{G}_f\mathbf{E}_f. \tag{A 13}$$

It is also known from Kalman filter theory that $\mathbf{E}_f$ is uncorrelated to $\mathbf{Z}_p$. Consequently, the noise term $\mathbf{E}_f$ can be removed by multiplying (from the right) equation (A 13) by $\mathbf{Z}_p^T$ which yields

$$\mathbf{Y}_f\mathcal{P}^{\perp}_{U_f}\mathbf{Z}_p^T = \mathcal{H}_{fp}\mathbf{Z}_p\mathcal{P}^{\perp}_{U_f}\mathbf{Z}_p^T, \tag{A 14}$$

and

$$\mathcal{H}_{fp}\mathbf{Z}_p = \mathbf{Y}_f\mathcal{P}^{\perp}_{U_f}\mathbf{Z}_p^T(\mathcal{P}^{\perp}_{U_f}\mathbf{Z}_p^T)^{-1}. \tag{A 15}$$

Finally, from equation A 8 we obtain that $\mathcal{H}_{fp}\mathbf{Z}_p = \mathcal{O}_f\mathbf{X}(n)$. Assuming that the input $u(n)$ is sufficiently rich in temporal behavior to excite all the observable dynamics of the system, matrix $\mathbf{X}(n)$ is ensured to be full row-ranked. In addition, $\mathcal{O}_f$ has full column-rank under the assumption of full observability. These properties suggest applying a singular value decomposition (SVD): (i) to determine the order of the identified system as the rank of $\mathcal{O}_f\mathbf{X}(n)$ and (ii) to isolate $\mathcal{O}_f$. Mathematically, this amounts to

$$\mathcal{H}_{fp}\mathbf{Z}_p = \begin{pmatrix} \mathcal{U}_1 & \mathcal{U}_2 \end{pmatrix} \begin{pmatrix} \mathcal{S}_1 & 0 \\ 0 & \mathcal{S}_2 \end{pmatrix} \begin{pmatrix} \mathcal{V}_1^T \\ \mathcal{V}_2^T \end{pmatrix}, \tag{A 16}$$

where the diagonal matrix $\mathcal{S}$ has been partitioned so that $\mathcal{S}_2$ is negligible compared to $\mathcal{S}_1$.

The size of $\mathcal{S}_1$ then represents the order of the identified system. Moreover, the extended observability matrix $\mathcal{O}_f$ can be extracted according to

$$\mathcal{O}_f = \mathcal{U}_1 \mathcal{S}_1^{1/2}. \tag{A 17}$$

A.3. *Extraction of the system matrices*

Based on $\mathcal{O}_f$, two different approaches may be adopted to extract the system matrices. The first one, denoted as *estimation focus*, extracts only the system matrices $\mathcal{A}$, $\mathcal{B}$, $\mathcal{C}$ and $\mathcal{D}$ from the data. On the other hand, if the noise covariances are needed, a more complex algorithm, a *simulation focus technique*, is called for. In this article, we will briefly introduce the first approach, while a detailed description of the second one can be found in Van Overschee & De Moor (1994), Van Overschee & De Moor (1996) or Juillet *et al.* (2013).

The first step consists in extracting the matrices $\mathcal{A}$ and $\mathcal{C}$ from $\mathcal{O}_f$. This can be accomplished rather easily by computing the matrix $\mathcal{O}_{f-1}$ as previously done with $\mathcal{O}_f$ and by recalling that, by definition, both matrices are related by the equation

$$\begin{pmatrix} \mathcal{I} & 0 \\ 0 & \mathcal{O}_{f-1} \end{pmatrix} \begin{pmatrix} \mathcal{C} \\ \mathcal{A} \end{pmatrix} = \mathcal{O}_f, \tag{A 18}$$

which can be solved by least-squares techniques. To determine the remaining matrices $\mathcal{B}$ and $\mathcal{D}$, one uses the fact that the problem is linear in these matrices; a simple least-squares matching to the output data may be used to find the remaining matrices (Van Overschee & De Moor (1996)).

REFERENCES

Adrian, R.J. 1979 Conditional eddies in isotropic turbulence. *Phys. Fluids* **22**, 2065–2070.

Bagheri, S., Brandt, L. & Henningson, D.S. 2009 Input–output analysis, model reduction and control of the flat-plate boundary layer. *J. Fluid Mech.* **620** (1), 263–298.

Barbagallo, A., Sipp, D. & Schmid, P.J. 2009 Closed-loop control of an open cavity flow using reduced-order models. *J. Fluid Mech.* **641** (1), 1–50.

Bergmann, M., Bruneau, C.-H. & Iollo, A. 2009 Enablers for robust pod models. *J. Comp. Phys.* **228** (2), 516–538.

Bonnet, J.-P., Cole, D.R., Delville, J., Glauser, M.N. & Ukeiley, L.S. 1994 Stochastic estimation and proper orthogonal decomposition: complementary techniques for identifying structure. *Exp. Fluids* **17**, 307–314.

Burl, J. B. 1999 *Linear Optimal Control*. Addison-Wesley Longman Publishing Co., Inc.

Butler, K. M. & Farrell, B. F. 1992 Three-dimensional optimal perturbations in viscous shear flow. *Physics of Fluids A: Fluid Dynamics (1989-1993)* **4** (8), 1637–1650.

Dergham, G., Sipp, D. & Robinet, J. C. 2013 Stochastic dynamics and model reduction of amplifier flows: the backward facing step flow. *J. Fluid Mech.* **719**, 406–430.

Guezennec, Y.G. 1989 Stochastic estimation of coherent structures in turbulent boundary layers. *Phys. Fluids* **1**, 1054–1060.

Hervé, A., Sipp, D., Schmid, P.J. & Samuelides, M. 2012 A physics-based approach to flow control using system identification. *J. Fluid Mech.* **702**, 26–58.

Hudy, L.M., Naguib, A. & Humphreys, W.M. 2007 Stochastic estimation of a separated flow field using wall-pressure array measurements. *Phys. Fluids* **19**, 024103.

Juillet, F., Schmid, P.J. & Huerre, P. 2013 Control of amplifier flows using subspace identification techniques. *J. Fluid Mech.* **725**, 522–565.

Kim, J. & Bewley, T. R. 2007 A linear systems approach to flow control. *Annu. Rev. Fluid Mech.* **39**, 383–417.

Lewis, J.M., Lakshmivarahan, S. & Dhall, S. 1989 Dynamic data assimilation: a least squares approach. In *Encyclopedia of Mathematics and Its Application 104*, , vol. 13. Cambridge University Press.

Ljung, L. 1999 *System identification: theory for the user*. Prentice Hall PTR.

Lumley, J. L. 1967 The structure of inhomogeneous turbulent flows. *Atmospheric turbulence and radio wave propagation* pp. 166–178.

Moore, B. 1981 Principal component analysis in linear systems: Controllability, observability, and model reduction. *Automatic Control, IEEE Transactions on* **26** (1), 17–32.

Qin, S.J. 2006 An overview of subspace identification. *Comp. & Chem. Eng.* **30** (10), 1502–1513.

Rowley, C. W. 2005 Model reduction for fluids, using balanced proper orthogonal decomposition. *International Journal of Bifurcation and Chaos* **15** (03), 997–1013.

Rowley, C. W. & Juttijudata, V. 2005 Model-based control and estimation of cavity flow oscillations. In *Decision and Control, 2005 and 2005 European Control Conference. CDC-ECC'05. 44th IEEE Conference on*, pp. 512–517. IEEE.

Sirovich, L. 1987 Turbulence and the dynamics of coherent structures. *Q. Appl. Math.* **45**, 561–571.

Taylor, J. A. & Glauser, M. N. 2004 Towards practical flow sensing and control via pod and lse based low-dimensional tools. *Journal of fluids engineering* **126** (3), 337–345.

Tinney, C.E., Coiffet, F., Delville, J., Hall, A.M., Jordan, P. & Glauser, M.N. 2006 On spectral linear stochastic estimation. *Exp. Fluids* **41**, 763–775.

Tu, J. H., Griffin, J., Hart, A., Rowley, C. W., Cattafesta III, L. N. & Ukeiley, L. S. 2013 Integration of non-time-resolved piv and time-resolved velocity point sensors for dynamic estimation of velocity fields. *Experiments in fluids* **54** (2), 1–20.

Van Overschee, P. & De Moor, B. 1994 N4SID: Subspace algorithms for the identification of combined deterministic-stochastic systems. *Automatica* **30** (1), 75–93.

Van Overschee, P. & De Moor, B. 1996 *Subspace identification for linear systems*. Kluwer.